nature geoscience

LETTERS

PUBLISHED ONLINE: 5 SEPTEMBER 2016 | DOI: 10.1038/NGEO2794

Coupling of turbulent and non-turbulent flow regimes within pyroclastic density currents

Eric C. P. Breard[1]*, Gert Lube[1]*, Jim R. Jones[2], Josef Dufek[3], Shane J. Cronin[4], Greg A. Valentine[5] and Anja Moebis[1]

Volcanic eruptions are at their most deadly when pyroclastic density currents sweep across landscapes to devastate everything in their path[1,2]. The internal dynamics underpinning these hazards cannot be directly observed[3]. Here we present a quantitative view inside pyroclastic density currents by synthesizing their natural flow behaviour in large-scale experiments. The experiments trace flow dynamics from initiation to deposition, and can explain the sequence and evolution of real-world deposits. We show that, inside pyroclastic density currents, the long-hypothesized non-turbulent underflow and fully turbulent ash-cloud regions[4,5] are linked through a hitherto unrecognized middle zone of intermediate turbulence and concentration. Bounded by abrupt jumps in turbulence, the middle zone couples underflow and ash-cloud regions kinematically. Inside this zone, strong feedback between gas and particle phases leads to the formation of mesoscale turbulence clusters. These extremely fast-settling dendritic structures dictate the internal stratification and evolution of pyroclastic density currents and allow the underflows to grow significantly during runout. Our experiments reveal how the underflow and ash-cloud regions are dynamically related—insights that are relevant to the forecasting of pyroclastic density current behaviour in volcanic hazard models.

For more than 50 years, the transport and deposition of pyroclastic density currents (PDCs) have remained amongst the most hotly debated issues in volcanology[1,5–7]. Due to their unpredictability and extreme violence, PDC deposits have been relied upon to infer flow dynamics[4,8]. PDC deposits range from massive to highly stratified types[9,10]. These extremes led to the conceptualization of two endmembers of PDC transport, one as a dry granular or gas-fluidized granular flow of high particle concentration[5,11,12], and the other as a dilute fully turbulent gravity current[13,14]. Attempts have been made to unify these endmembers, both theoretically[15] and with numerical modelling studies[16]. However, large uncertainties remain about the multiphase physics of coupled concentrated/dilute particle-gas transport[17]. Thus, even conceptual paradigms of the internal structure of PDCs remain highly controversial[4], and envisage either rigid, coexisting zones of concentrated laminar and dilute fully turbulent transport regimes[6–8], or a continuous gradation between them[9,10].

Here we report on gas–particle flows produced by the gravitational collapse of 1.5 tons of volcanic material (Methods, Supplementary Fig. 1 and Supplementary Movie 1). As in nature, experimental currents of pumice, ash and air were synthesized by 'eruption column collapse' of mixtures of natural volcanic particles and air, which impacted onto an inclined channel[18] (Fig. 1). The resultant flows were dynamically and kinematically scaled to natural flows (Supplementary Tables 1–3). Experiments were conducted at ambient temperature (Supplementary Table 1). They thus exclude a late phase of buoyancy reversal as seen in hot natural flows. They travelled out to >25 m and were observed with high-speed cameras over several seconds of propagation.

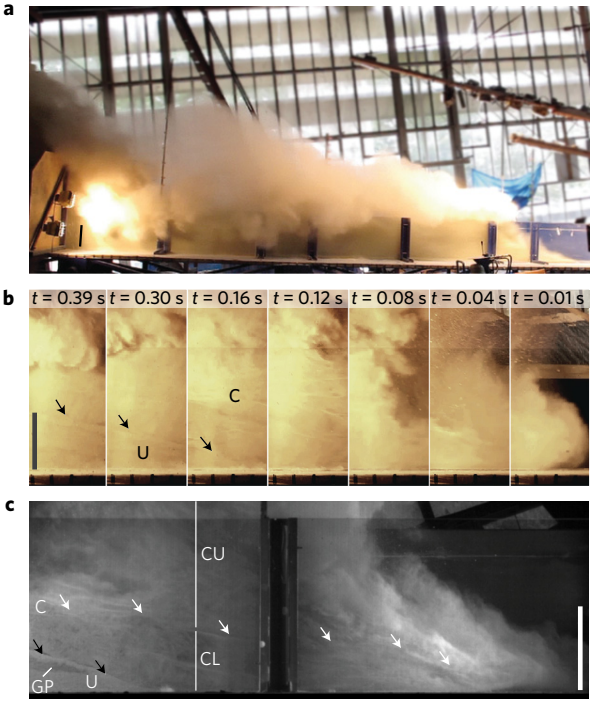

Figure 1 | Synthesizing pyroclastic density currents in large-scale experiments. a, Side view of an experimental pyroclastic density current at the eruption simulator PELE. **b**, Lower 0.95 m of the flow at a runout distance of 3 m at different times. **c**, Passage of the head region at 3 m. Arrows highlight the interfaces between underflow (U, lower zone) and ash-cloud regions (C) (black), and between middle (CL) and upper (CU) zones of the pyroclastic density current, respectively. Rapid sedimentation of dendritic clusters of mesoscale turbulence entraps gas pockets (GP) in the underflows. Vertical scaling bars are 0.3-m long.

[1]Volcanic Risk Solutions, Institute of Agriculture and Environment, Massey University, Private Bag 11 222, Palmerston North 4442, New Zealand. [2]School of Engineering and Advanced Technology, Massey University, Palmerston North 4442, New Zealand. [3]School of Earth and Atmospheric Science, Georgia Institute of Technology, 311 Ferst Drive, Atlanta, Georgia 30332, USA. [4]School of Environment, The University of Auckland, 3A Symonds St, Auckland 1010, New Zealand. [5]Department of Geology, State University of New York, University at Buffalo, 411 Cooke Hall, Buffalo, New York 14260-1350, USA.
*e-mail: e.c.p.breard@massey.ac.nz; g.lube@massey.ac.nz

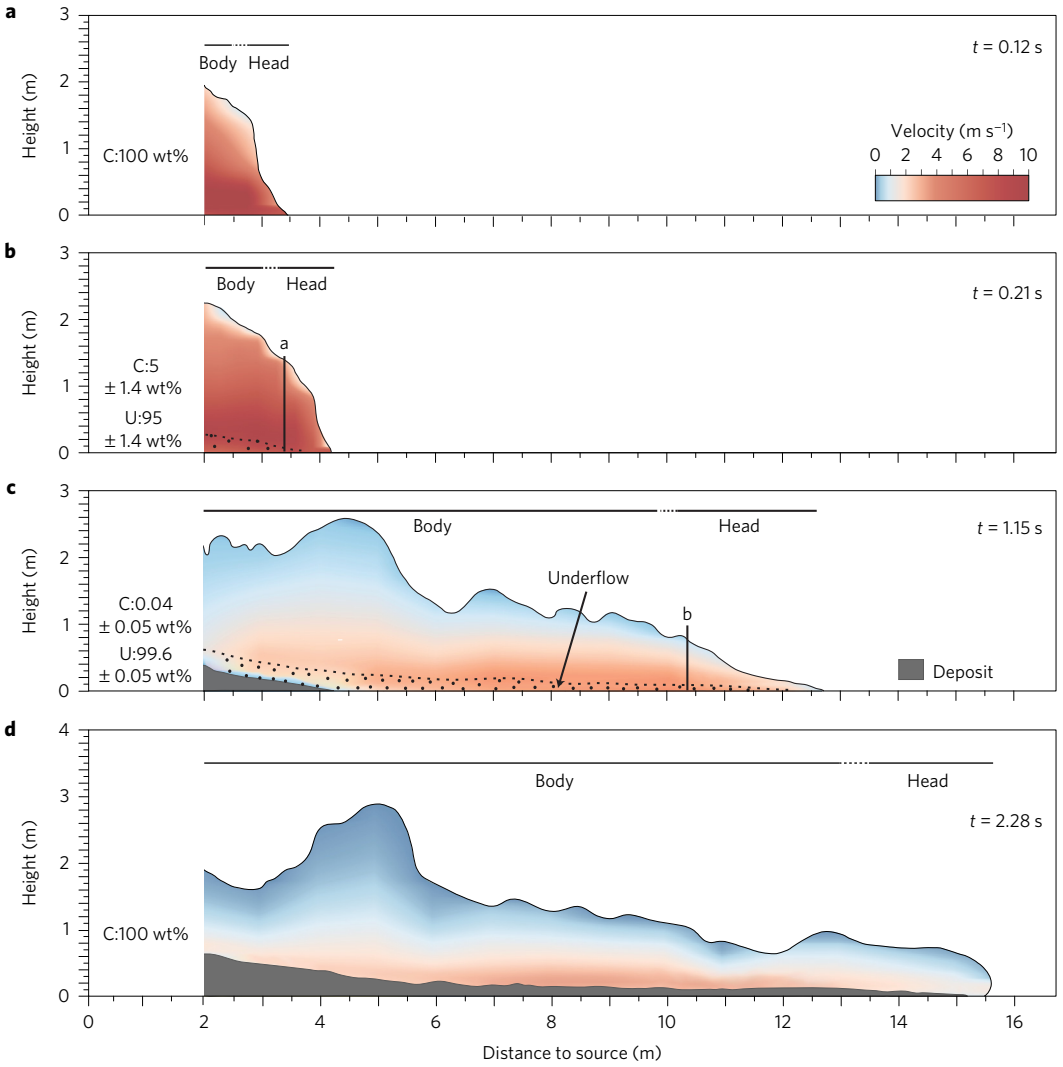

Figure 2 | Evolution of the internal flow structure and velocity fields. a–d, Longitudinal cross-sections of the advancing experimental PDC at four different times. Black solid line, dotted line and grey area demark upper flow boundary, top of underflow and aggrading deposit, respectively. Extents of head and body regions of ash-cloud and relative proportions of the mass of particles transported in underflow (U) and ash-cloud (C) regions are shown also. Two vertical lines annotated 'a' and 'b' indicate the location of the proximal and intermediate observer locations referred to in Fig. 4.

Upon impact, the fully turbulent suspension rapidly expanded and accelerated to reach initial velocities of 16 m s^{-1} (Fig. 2a). This was short-lived, and by at least 3.1 m from source (Fig. 2b and Supplementary Movie 2), the initially homogeneous suspension (containing 9.5 vol% particles) had vertically segregated into a basal underflow and an overriding ash-cloud. After this initial segregation event, 95 ± 1.4% of the mass was transported in the underflow, reaching 99.6 ± 0.05% by 10.3 m from source (Fig. 2c). The ash-cloud also segregated longitudinally into a gravity current with a highly inertial head (Froude numbers 1.4–3) and a trailing body where inertial and gravitational forces balanced (Froude numbers 0.9–1.2). The head comprised a leading section that preceded the underflow and a rear section that rode atop of it, while the body moved on top of the remaining underflow (Fig. 2). These segregation processes generated flow regions of markedly contrasting (depth- and time-averaged) particle concentrations. During passage of the current at 3.1 m, the underflow was the most concentrated region at 45 ± 0.045 vol% particles. The head contained 5.5 ± 0.05 × 10^{-1} vol% particles, while the body transported 8 ± 0.08 × 10^{-2} vol% particles. Further downstream at 10.6 m, the head and body regions were each diluted by an order of magnitude due to sedimentation and entrainment, while the concentration of the underflow remained high.

The vertical and longitudinal flow segregations link sediment transport to deposit characteristics. The ash-cloud head emplaced the earliest and farthest reaching depositional unit. Deposited from 9–25 m in ~0.3 s and at a deposition rate of ~3.5 mm s^{-1} (Unit 1 in Fig. 3a,b), this unit was a thin and crudely laminated layer, rich in high-density particles. This was directly overlain by the deposit of the underflow (Unit 2), which reached a runout length of ~15.2 m. Vertical aggradation occurred at a fast rate of 450–550 mm s^{-1} (Fig. 3c), which is considerably higher than the aggradation rates reported in small-scale experiments on dry granular and fluidized granular flows[19,20]. This rapid 'freezing' occurred only in the last instance of underflow emplacement, when the characteristic and high slip velocity at the lower flow boundary (Fig. 3c) ceased and left a deposit representing a snapshot of the underflow's structure in motion. The underflow deposit depicts a fines-rich base, followed by a massive central portion and coarse pumice-rich top. The ash-cloud body, which during segregation became enriched in very fine and low-density ash particles, formed an up to ~8-m high and ~24-m long cloud that was deposited last. The normally graded and thinly laminated unit 3 initially

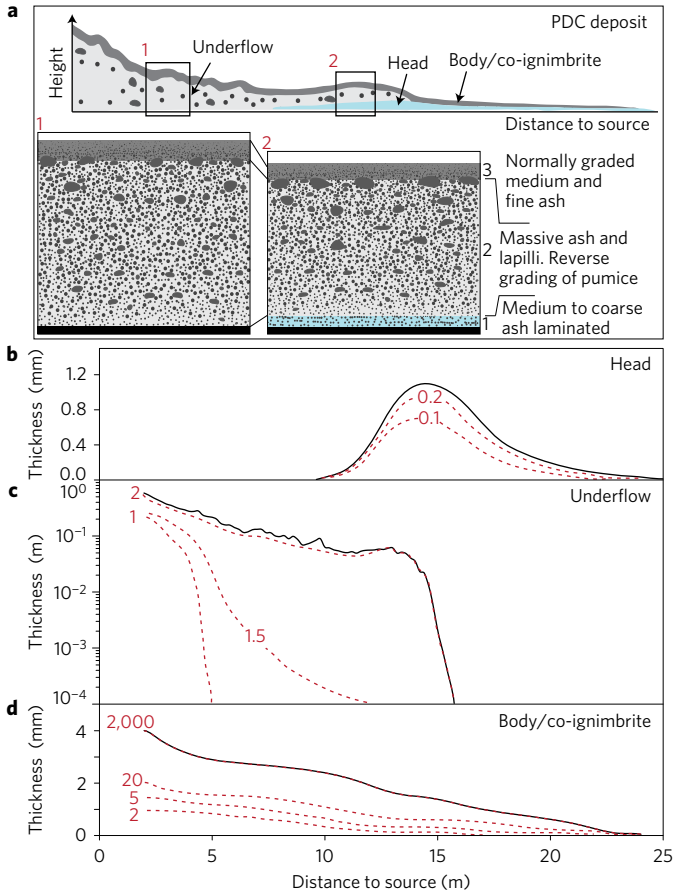

Figure 3 | Experimental deposit and timescale of deposition. a, Sketch of the experimental deposit sequence (not to scale) correlating the three depositional units to the parent zones of the flow (head, underflow, body/co-ignimbrite). Two stratigraphic sections '1' and '2' highlight the sediment structure, with the standard ignimbrite flow unit deposited only in an intermediate runout zone. **b**–**d**, Thickness–distance plot (black line) and isochrones of deposition after flow front arrival (red dashed lines, in seconds) for the head, underflow and body regions, respectively.

deposited at a rate of 0.1–0.5 mm s^{-1}, which subsequently slowed to ~10^{-2} to 10^{-5} mm s^{-1} (Fig. 3d). Thus, the total PDC deposition timescale spanned five orders of magnitude, and was composed of three depositional units emplaced by the head, underflow and body regions.

The deposit structure of our large-scale experiments reproduced the natural sequence and sedimentary features of real-world deposits (Fig. 3). For the case of pumice-rich eruptions this classic tripartite sequence (composed of layers 1, 2 and 3) is referred to as the standard ignimbrite unit[5,21,22]. The similarity of natural and experimental grain-size distributions can be visualized in a graph of the median grain-size diameter against the sorting coefficient. Median-sorting data for experimental units 1, 2 and 3 plot within the established fields of layers 1, 2 and 3, respectively, of ignimbrite deposits (Supplementary Fig. 2a). In vertical sections through the tripartite experimental deposits, the variation of the median diameters and sorting coefficients shows the same trends as natural sequences (Supplementary Fig. 2b–d), suggesting similar processes of flow segregation, gas–particle transport and deposition.

The footprints of the three depositional units associated with the underflow and the head and body regions of the ash-cloud only partially overlap (Fig. 3a). This gives an explanation of why the 'ground layer'[23] of PDC deposits is locally absent in some natural deposit sequences, but is present in others[4,5,24].

While the head, underflow and body regions emplaced distinguishable depositional units, the three flow regions do not move and evolve independently. This is best shown through high-resolution vertical profiles of velocity, particle concentration and vorticity (a measure of the degree of turbulence) during passage of the rear of the ash-cloud head (Fig. 4a). At this point, the flow shows three zones of contrasting turbulence: a lower, 0.1-m thick, laminar zone (Reynolds numbers, Re of 10^0–10^1), representing the underflow; a middle 0.2–0.4-m-thick zone of intermediate turbulence (Re of 10^3) representing the lower part of the ash-cloud (CL in Fig. 4); and an upper 1.1-m-thick, fully turbulent zone of the ash-cloud (Re of 10^4–10^5; CU in Fig. 4). A sharp concentration change between the lower and middle zones occurred over only a few millimetres (Supplementary Movie 3), where particle concentrations declined abruptly from ~20 to 2 vol%. However, this was not accompanied by a sharp velocity change, which instead changed smoothly across this interface (Fig. 4a), and so demonstrates an efficient momentum transfer from the underflow into the ash-cloud. The change in Reynolds number across this interface from ~18 to ~4,000 translates into an abrupt increase in vorticity from low to intermediate values (Fig. 4a). The middle zone is also characterized by low shear and the particle concentration is relatively height invariant between 1 and 2.5 vol% (Fig. 4a). In contrast, the upper zone shows high vorticity as the flow becomes fully turbulent. In the upper ash-cloud, particle concentration and velocity declined strongly upwards, which resulted in strong shear and subsequent intense billowing. The rapid changes in concentration, velocity and vorticity between the middle and upper zones occurred across a broad interface of several centimetres in thickness.

In the middle zone, the ratio of the eddy rotation time and the particle response time to unsteady forcing by gas turbulence (the Stokes number)[15] is above unity (1.5–5). The stability number[15], a measure of the residence time of solids in an eddy, is close to unity (0.25–1.1). This is a condition discovered in multiphase physics that favours strong feedback between solid and gas phases[25–27]. The feedback leads to the formation of mesoscale turbulence structures where particles associate in a dendritic pattern, and migrate into low-shear zones[26]. Such mesoscale structures are highly abundant in the middle zone (Supplementary Note 1 and Supplementary Figs 3–5). They occur as dendritic clusters of higher particle concentration than the surrounding mixture, and strongly affect flow stratification and sedimentation (Fig. 1c, Supplementary Movie 3, and Supplementary Fig. 3). By contrast, the upper zone is devoid of mesoscale structures and Stokes and Stability numbers rapidly decline to values of 10^{-2} and 10^{-1}, respectively, while Reynolds numbers increase up to 10^6. This indicates highly turbulent transport with well-mixed and coupled solid and gas phases.

The discovery of mesoscale clusters in PDCs has major ramifications for the exchange of mass between zones and the consequent runout dynamics. They are known to dampen local turbulence and to force a local decrease of particle drag coefficients[25]. This process effectively counters the high aerodynamic resistance expected in (viscous) concentrated suspensions through hindered settling[28].

In fact, the low-shear middle zone had extremely high particle settling velocities of ~1.7 m s^{-1} (Fig. 4a and Supplementary Fig. 3). These velocities are considerably higher than estimates of particle settling velocities[29] for hindered settling in a dusty gas (that is, 0.35–0.4 m s^{-1}; refs 28,30, see Methods).

The high particle settling rate implies a thickening of the underflow at 60 ± 10 mm s^{-1} (Methods). The mass flux from ash-cloud onto underflow regions between 3.1 and 10.6 m from source is illustrated by downward velocity components (Fig. 4). This resulted in a strong dilution of the ash-cloud head and frontal body regions (0.55–0.08 vol%), where the middle zone was thickest and

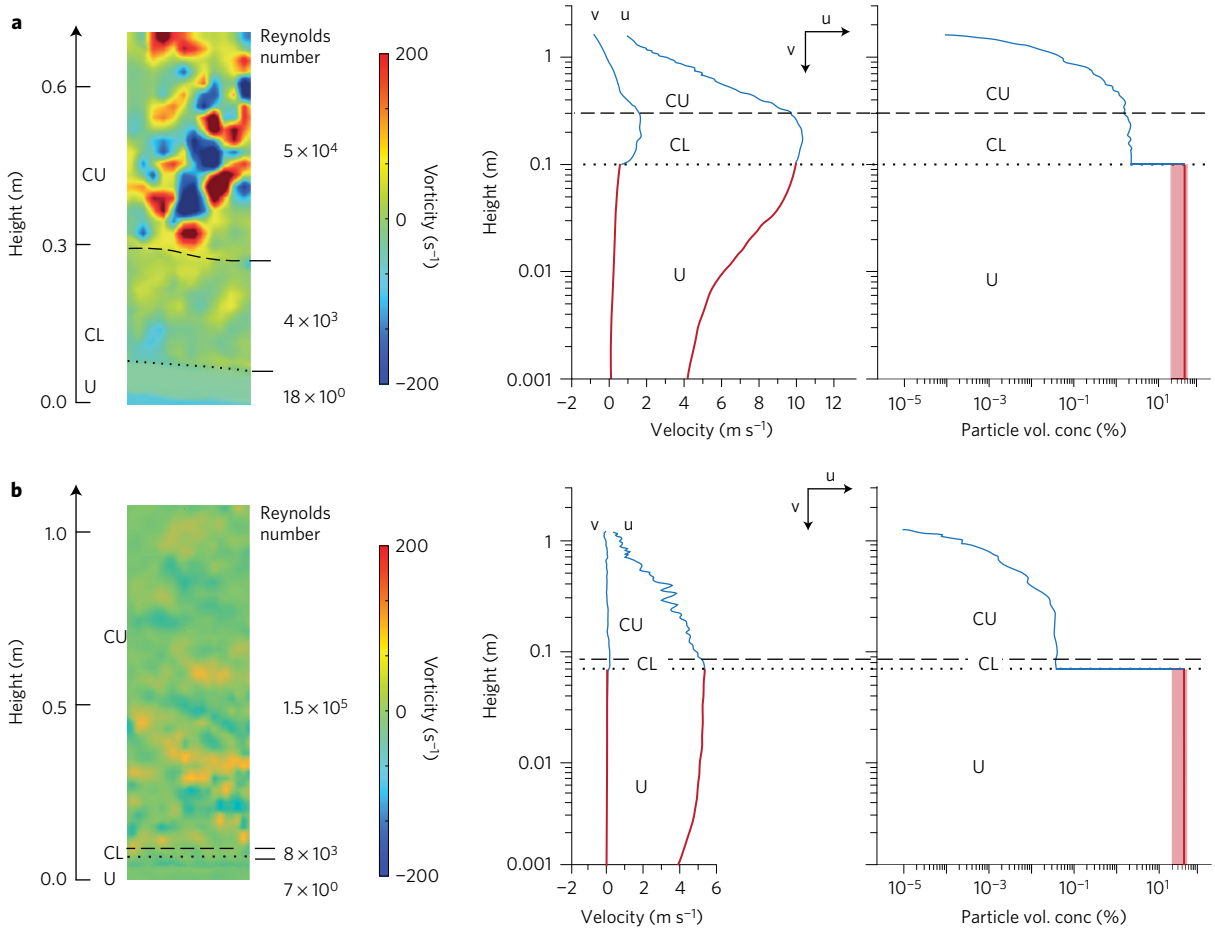

Figure 4 | Internal structure of experimental PDCs. a, Vertical profiles of vorticity (vertical colour scales give the intensities), horizontal and vertical velocity components, and particle concentration at 3.1 m from source during passage of the rear of the head. **b**, Same as **a**, but at a runout distance of 10.6 m. Dotted and dashed lines demarcate interfaces between lower (U), middle (CL) and upper (CU) zones of the flow, respectively, with their depth-averaged Reynolds numbers given also. For the underflow, red solid lines show depth-averaged particle concentrations. Light-red bar indicates maxima (in the central part) and minima (base and top of underflow).

transported the coarsest particle sizes. This fast-settling process of mesoscale clusters increased the mass of the underflow by ~5%. Translated to natural PDC scales, this indicates a significant mass flux from the ash-cloud into the underflow; for example, resulting in underflow thickening by 1.8 m during 30 s of propagation and 36 m in 10 min. In other words, the PDC head constantly feeds the frontal part of the advancing underflow. The associated momentum transfer promotes the high mobility of the coupled head–underflow system.

Viewing inside pyroclastic density currents establishes a relationship between flow behaviour and deposit architecture. Ash-cloud and underflow regimes are spatially separated, but strongly coupled through a regime of intermediate particle concentration and turbulence. Importantly, this coupling controls the velocity and density stratification, and consequently the generation of damaging dynamic pressures in PDCs. The spectrum of particle-gas transport between concentrated and dilute endmembers is complex in that regime of intermediate concentration, which is characterized by formation of dense mesoscale clusters. The clusters behave differently from individual dispersed particles (dilute) or dense granular dispersions (concentrated). This generates a tripartite vertical PDC zonation, where zone boundaries are demarcated by abrupt changes in turbulence intensity and in the degree of coupling between gas and particle phases. The recognition of mesoscale structures and coupling between concentrated and dilute transport regions reveals fundamental processes that control the enigmatic internal dynamics and hazards of pyroclastic density currents. Our results also suggest that a hot carrier phase is not necessary to confer to PDCs their unique characteristics (complexity of deposits, long runout and rapid segregation). Thus, these processes may be similarly relevant to other types of terrestrial non-volcanic mass flows.

Methods

Methods, including statements of data availability and any associated accession codes and references, are available in the online version of this paper.

Received 25 February 2016; accepted 22 July 2016; published online 5 September 2016

References

1. Francis, P. W. & Baker, M. C. W. Mobility of pyroclastic flows. *Nature* **270,** 164–165 (1977).
2. Fink, J. H. & Kieffer, S. W. Estimate of pyroclastic flow velocities resulting from explosive decompression of lava domes. *Nature* **363,** 612–615 (1993).
3. Dufek, J., Esposti Ongaro, T. & Roche, O. in *The Encyclopedia of Volcanoes* 2nd edn (ed. Sigurdsson, H.) 617–629 (Academic, 2015).
4. Branney, M. & Kokelaar, P. *Pyroclastic Density Currents and the Sedimentation of Ignimbrites* Vol. 27 (Geological Society Publishing House, 2002).
5. Sparks, R. S. J. Grain size variations in ignimbrites and implications for the transport of pyroclastic flows. *Sedimentology* **23,** 147–188 (1976).
6. Dade, W. B. & Huppert, H. E. Emplacement of the Taupo ignimbrite by a dilute turbulent flow. *Nature* **381,** 509–512 (1996).

7. Sparks, R. S. J., Wilson, L. & Hulme, G. Theoretical modeling of the generation, movement, and emplacement of pyroclastic flows by column collapse. *J. Geophys. Res. Solid Earth* **83,** 1727–1739 (1978).
8. Fisher, R. V. & Schmincke, H. U. *Pyroclastic Rocks* (Springer, 1984).
9. Fisher, R. V. Models of pyroclastic surges and pyroclastic flows. *J. Volcanol. Geotherm. Res.* **6,** 305–318 (1979).
10. Valentine, G. A. & Fisher, R. V. in *Encyclopedia of Volcanoes* (eds Sigurdsson, H. *et al*.) 571–580 (Academic, 2000).
11. Wilson, C. J. N. The role of fluidization in the emplacement of pyroclastic flows: an experimental approach. *J. Volcanol. Geotherm. Res.* **8,** 231–249 (1980).
12. Roche, O. Depositional processes and gas pore pressure in pyroclastic flows: an experimental perspective. *Bull. Volcanol.* **74,** 1807–1820 (2012).
13. Valentine, G. A. Stratified flow in pyroclastic surges. *Bull. Volcanol.* **49,** 616–630 (1987).
14. Bursik, M. I. & Woods, A. W. The dynamics and thermodynamics of large ash flows. *Bull. Volcanol.* **58,** 175–193 (1996).
15. Burgisser, A. & Bergantz, G. W. Reconciling pyroclastic flow and surge: the multiphase physics of pyroclastic density currents. *Earth Planet. Sci. Lett.* **202,** 405–418 (2002).
16. Neri, A., Esposti Ongaro, T., Macedonio, G. & Gidaspow, D. Multiparticle simulation of collapsing volcanic columns and pyroclastic flow. *J. Geophys. Res. Solid Earth* **108,** 2202 (2003).
17. Dufek, J. The fluid mechanics of pyroclastic density currents. *Annu. Rev. Fluid Mech.* **48,** 459–485 (2016).
18. Lube, G., Breard, E. C. P., Cronin, S. J. & Jones, J. Synthesizing large-scale pyroclastic flows: experimental design, scaling, and first results from PELE. *J. Geophys. Res. Solid Earth* **120,** 1487–1502 (2015).
19. Girolami, L., Druitt, T. H. & Roche, O. Towards a quantitative understanding of pyroclastic flows: effects of expansion on the dynamics of laboratory fluidized granular flows. *J. Volcanol. Geotherm. Res.* **296,** 31–39 (2015).
20. Lube, G., Huppert, H. E., Sparks, R.S. J. & Freundt, A. Granular column collapses down rough, inclined channels. *J. Fluid Mech.* **675,** 347–368 (2011).
21. Sparks, R. S. J., Self, S. & Walker, G. P. L. Products of ignimbrite eruptions. *Geology* **1,** 115–118 (1973).
22. Freundt, A. & Schmincke, H. U. Emplacement of small-volume pyroclastic flows at Laacher See (East-Eifel, Germany). *Bull. Volcanol.* **48,** 39–59 (1986).
23. Sparks, R. S. J. & Walker, G. P. L. The Ground Surge Deposit: a third type of pyroclastic rock. *Nat. Phys. Sci.* **241,** 62–64 (1973).
24. Palladino, D. M. & Valentine, G. A. Coarse-tail vertical and lateral grading in pyroclastic flow deposits of the Latera Volcanic Complex (Vulsini, central Italy): origin and implications for flow dynamics. *J. Volcanol. Geotherm. Res.* **69,** 343–343 (1995).
25. Zhang, D. Z. & VanderHeyden, W. B. The effect of mesoscale structures on the macroscopic momentum equations for two phase flows. *Int. J. Multiph. Flow* **28,** 805–822 (2002).
26. Agrawal, K., Loezos, P. N., Syamlal, M. & Sundaresan, S. The role of meso-scale structures in rapid gas–solid flows. *J. Fluid Mech.* **445,** 151–185 (2001).
27. Burgisser, A., Bergantz, G. W. & Breidenthal, R. E. Addressing complexity in laboratory experiments: the scaling of dilute multiphase flows in magmatic systems. *J. Volcanol. Geotherm. Res.* **141,** 245–265 (2005).
28. Gidaspow, D. *Multiphase Flow and Fluidization: Continuum and Kinetic Theory Description* (Academic, 1994).
29. Dellino, P. *et al*. The analysis of the influence of pumice shape on its terminal velocity. *Geophys. Res. Lett.* **32,** L21306 (2005).
30. Syamlal, M. & O'Brien, T. J. Computer simulation of bubbles in a fluidized bed. *AIChE Symp. Ser.* 22–31 (1989).

Acknowledgements

We are very grateful to G. Kereszturi and R. van Niekerk for assisting with the experiments. We thank S. Sundaresan for helpful discussions regarding mesoscale clusters and A. Freundt for his help on the Laacher See ignimbrites. We also thank K. Arentsen and B. Walsh for internal reviews. This study was partially supported by the Royal Society of New Zealand Marsden Fund (contract no. 15-MAU-085) and the New Zealand Natural Hazards Research Platform (contract no. 2015-MAU-02-NHRP). We are very grateful to A. Neri and A. Burgisser for thoughtful reviews that strengthened the manuscript.

Author contributions

E.C.P.B. and G.L. designed the experiments and wrote the first draft of the manuscript, which was then revised by all the authors. E.C.P.B. and G.L. conducted the experiments with the help of A.M., who also assisted in the mixture density measurements. E.C.P.B. led the data analyses and their interpretation, assisted by G.L., J.R.J., J.D., S.J.C. and G.A.V. G.L. designed the experimental facility with the help of J.R.J. and S.J.C. All authors concurred with the paper's content.

Additional information

Supplementary information is available in the online version of the paper. Reprints and permissions information is available online at www.nature.com/reprints. Correspondence and requests for materials should be addressed to E.C.P.B. or G.L.

Competing financial interests

The authors declare no competing financial interests.

Methods

Generating pyroclastic density currents (PDCs) in large-scale experiments. Our experiments were conducted at the eruption simulator PELE (described in detail in ref. 18), a unique test facility to synthesize the natural behaviour of PDCs. The experimental PDCs of up to six tons of natural volcanic material and air attain velocities of 7–32 m s^{-1}, flow thicknesses of 2–4.5 m, and runout lengths of >35 m (ref. 18). The particle-gas currents are synthesized by the gravitational collapse of variably concentrated suspensions of volcanic particles and air from an elevated hopper onto an instrumented runout section. PELE is operated inside a 16-m high, 25-m long and 18-m wide disused boiler house and comprises: a 13-m high tower and elevator holding a 4.2 m^3 hopper through which a pyroclastic mixture is discharged at variable discharge height; a shrouded, fall section (up to 9 m) below the suspended hopper; a 12-m long, 0.5-m wide and 0.6-m high inclinable channel section with a rough steel base (basal friction angle of 36.5°); and a 30-m long flat runout area of concrete (basal friction angle of 37.5°) that extends outside the building. Experiments were undertaken at ambient temperature, with an eruption column fall height of 3 m, a constant hopper discharge rate of 825 kg s^{-1}, and with the channel uniformly sloping at 19°.

The experimental particle mixture was prepared by blending two different deposits of the AD 232 Taupo Ignimbrite[18]. The mixture had a unimodal grain-size distribution with a median diameter of 250 μm, an average clast density of 1,950 kg m^{-3}, and contained 10 wt% of very fine ash material (particles <63 μm) (Supplementary Fig. 1).

Additional details of the experimental set-up, the experimental protocol, properties of the volcanic material and measurement techniques are provided in ref. 18, while some analytical methods specific to our results requiring further explanation are given below.

The experimental conditions of the experimental run described in this letter are summarized in Supplementary Table 3. The here documented processes of flow segregation into lower, intermediate and upper zones of characteristic particle concentration and turbulence are not restricted to these starting conditions. Supplementary Table 3 thus also reports the tested wider range of starting conditions under which qualitatively similar flow structures are produced. This range of starting conditions includes those tested in experiment PF_10_5 of ref. 18. A main difference between the experiments described here and those documented in ref. 18, however, is the availability and analyses of detailed velocity, concentration and turbulence intensity data.

Sensors and analytical methods. Two high-speed cameras operated at 600–1,000 frames per second, and four normal-speed cameras operated at 24–240 frames per second, recorded flow passing and sedimentation from a range of viewing angles. Two-dimensional velocity and vorticity fields were computed via particle image velocimetry (PIV) using the software PIVlab[31]. Vorticity measurements reported in Fig. 4 use a smallest interrogation window of 0.04 m that represents the minimum length scale of eddies displayed in the 2D vorticity plot.

Continuous vertical profiles of particle concentration of the ash-cloud were obtained using an optical method. This method makes use of an empirical relationship between the local median grey scale of high-speed images and the local particle volume concentration of the gas–particle mixture. The validity of the empirical relationship and the minimum range of quantifiable concentrations (approximately 10^{-5}–10^{1}%) were confirmed through direct measurements of the time-variant concentration of the gas–particle mixture[18]. Here, particle volumetric concentration C_p is defined as:

$$C_p = \frac{\frac{V_e}{t}(1-\varepsilon)}{\rho_p A_s} \quad (1)$$

where V_e is the time-variant volume of sediment accumulating in transparent sediment samplers during short regular time intervals t (=0.05 s), ε is the porosity of the deposit in the sampler during each time interval t, ρ_p is the average particle density of the sediment captured in the sampler during each time interval t, and A_s is the cross-sectional area of the sampler.

The empirical relationship between the median grey-scale and particle volumetric concentration takes the form:

$$C_p = a\,Md(\text{grey})^k \quad (2)$$

$Md(grey)$ is the median grey scale of the flow entering the sediment sampler, with a being an experimentally determined constant of 5×10^{-8}, while k is dependent on the local background illumination. The local value of k can be determined through iteration of the following equality:

$$\int_{t_0}^{t_f} v_S A_s a\,Md(\text{grey})^k \rho_s = m_e \quad (3)$$

where t_0 and t_f refer to the onset and cessation of sediment transport in the flow, ρ_s is the average particle density of the sediment, v_S is the time-variant velocity measured by PIV and averaged across the width of the passive transparent sediment, and m_e is the total mass collected in the sampler from t_0 to t_f.

The difference of mixture concentration measurements using the direct sediment sampling technique and the empirical optical method is less than 10% over the entire concentration range.

The particle volume concentrations of the ash-cloud head and body regions at 3.1 and 10.6 m from source reported in the main text were obtained by time- and depth-averaging of concentration data series during the passage of the ash-cloud head and body, respectively.

The density of the flow ρ (ash-cloud or underflow) can be estimated from the particle volumetric concentration C, the average particle density ρ_P, and air density ρ_a as follows:

$$\rho = C\rho_P + (1-C)\rho_a \quad (4)$$

The mass of the ash-cloud m_{AC_i} at a given time t_i during flow propagation was estimated from the average density of the ash-cloud ρ_{AC_i} and its volume V_{AC_i} at t_i:

$$m_{AC_i} = \rho_{AC_i} V_{AC_i} \quad (5)$$

The depth-averaged particle volumetric concentration of the underflow reported in the text was calculated as follows:

$$C_U = \frac{m_U}{A h_U \rho_P} \quad (6)$$

where A is the area of a loadcell measuring the total mass of flow passing at an observer location[18], h_U is the time-variant thickness of the underflow measured in high-speed videos, ρ_p is the average particle density, and m_U is the mass of the underflow. m_U was computed by subtracting the mass of the ash-cloud m_A from the total mass of the flow m_t.

The mass of the underflow m_{U_i} at a given time t_i during flow propagation was estimated from the average density of the underflow ρ_{U_i} and its volume V_{U_i} at t_i.

$$m_{U_i} = \rho_{U_i} V_{U_i} \quad (7)$$

Proportions of mass of the underflow $m_{U_{i(\%)}}$ and ash-cloud $m_{AC_i\%}$ reported in the main text and Fig. 2 for t_i = 0.12 s, 0.21 s, 1.15 s and 2.28 s, have been derived from the following equations:

$$m_{U_{i(\%)}} = \frac{m_{U_i}}{m_{U_i} + m_{AC_i}} \quad (8)$$

$$m_{U_{i(\%)}} = \frac{m_{AC_i}}{m_{U_i} + m_{AC_i}} \quad (9)$$

The maximum error attributed to the volume estimates is 5%. In combination with the maximum error of the concentration measurements of 10%, this gives a maximum error around the mass estimates m_{U_i} and m_{AC_i} of 15%. Owing to the nonlinearity of equation (4), the error around the mass estimates decreases with a decrease of particle volumetric concentration. Hence, the maximum errors around the mass proportion of the ash-cloud $m_{U_{i(\%)}}$ and underflow $m_{U_{i(\%)}}$ are also nonlinear and reported in Fig. 2 and in the main text.

Local rates of underflow thickening, T_U, reported in the text were directly measured in high-speed videos, but they can also be estimated as the ratio:

$$T_U = \frac{C_{LC} W_{LC}}{(1-\varepsilon)} \quad (10)$$

where C_{LC} and W_{LC} are the depth-averaged particle concentration and depth-averaged settling velocity in the lower 5% of the ash-cloud, and ε is the porosity of the underflow. As an example, during passage of the rear of the head at the observer location at 3.1 m, W_{LC} = 1.7 m s^{-1}, ε = 0.55, C_{LC} = 0.015 (Fig. 4a), resulting in T_U = 57 mm s^{-1}. This is in good agreement with direct measurements that give thickening rates of 60 ± 10 mm s^{-1}.

Values of the Reynolds number (Re^{**}) reported in the text and in Fig. 4 are defined as:

$$Re^{**} = \frac{\rho U H}{\mu^{**}} \quad (11)$$

where U and H are depth-averaged velocity and height of the flow, respectively; ρ is the depth-averaged flow density; and μ^{**} is the dynamic viscosity of the flow.

The dynamic viscosity μ^{**} in equation (11) is given by[32,33]:

$$\mu^{**} = \mu(1+M^*)^2 \quad (12)$$

where μ^{**} is the gas dynamic viscosity (μ) corrected for particle collisions:

$$M^* = \rho_p C_p / \rho_a (1 - C_p) \quad (13)$$

The flow density ρ can be related to the particle volumetric concentration C_p and the particle density ρ_p and air density ρ_a as follows:

$$\rho = \rho_a (1 - C_p) - \rho_p C_p \quad (14)$$

Values of the Stokes S_T and Stability Σ_T numbers reported in the text are defined as follows[15]:

$$S_T = \frac{U_T \Delta U_i}{g\delta} \quad (15)$$

$$\Sigma_T = \frac{U_T}{\Delta U_i} \quad (16)$$

where U_T is the terminal fall velocity of the time- and space-variant median grain size transported in the flow and δ is the eddy diameter, which were both measured by PIV analysis, ΔU_i is the eddy rotation velocity, and g is acceleration of gravity. ΔU_i was measured directly from the PIV and is in good agreement with the formulation of ref. 34.

The time- and space-variant median grain size transported in the flow was obtained by standard particle size analysis of the sediment samples collected in the passive transparent samplers.

Predicted settling velocity in the middle zone. The settling velocity w of particles through a fluid is described as follows[29]:

$$w = \frac{1.2065 \mu_f^{**} \left(\frac{D^3 g (\rho_s - \rho_f) \rho_f \Psi^{1.6}}{\mu^2} \right)^{0.5206}}{D \rho_f} \quad (17)$$

where Ψ is the shape factor, ρ_f is the fluid density, μ_f^{**} is the gas dynamic viscosity, and D the particle diameter. For the experimental mixture, a shape factor of 0.5 was determined following ref. 29. The drag coefficient of a sphere of equivalent diameter can be estimated from the following equation:

$$C_D = \frac{4Dg(\rho_s - \rho_f)}{3\rho_f w^2} \quad (18)$$

where the symbols are equivalent to those in equation (17).

However, the mixture in the middle zone is highly concentrated, so that hindered settling will affect the particle drag coefficient, hence modifying the settling velocity of the particles. The Syamlal–O'Brien drag coefficient[30] that accounts for particle concentration of the mixture is defined as follows:

$$C_D = \left(0.63 + \frac{4.8}{\sqrt{\mathrm{Re}_p / u_{r,p}}} \right)^2 \quad (19)$$

where

$$u_{r,p} = 0.5(A - 0.06\mathrm{Re}_p + \sqrt{(0.06\mathrm{Re}_p)^2 + 0.12\mathrm{Re}_p(2B - A) + A^2}) \quad (20)$$

and

$$A = \alpha_g^{4.14} \quad B = \alpha_g^{2.65} \text{ (for } \alpha_g > 0.85) \quad (21)$$

The term α_g is the gas volumetric concentration and Re_p is the Reynolds particle number.

The particle Reynolds number is defined as follows[30]:

$$\mathrm{Re}_p = \frac{\rho_f D |\boldsymbol{u}_p - \boldsymbol{u}_f|}{\mu_f^{**}} \quad (22)$$

where $|\boldsymbol{u}_p - \boldsymbol{u}_f|$ is the relative velocity between particles settling and gas assumed to be the settling velocity w, D is the particle diameter, ρ_f is the fluid density, and μ_f^{**} is the dynamic viscosity of the fluid.

The Gidaspow drag coefficient model[28] also takes into account the particle concentration and is defined as follows:

$$C_D = \frac{24}{\mathrm{Re}_p}(1 + 0.15\mathrm{Re}_p^{0.687}) \quad \text{for } \mathrm{Re}_p \leq 1{,}000 \quad (23)$$

Fine particles couple with the gas phase to increase the mixture density and dynamic viscosity of the fluid[33], therefore increasing the drag. Using measurements of the settling velocities of lapilli-sized particles (4 m s^{-1} for particles with diameter of -2.5Φ and 2.5 m s^{-1} for particles with diameter of -3Φ) through the mixture at the observer location of 3.1 m and equation (17), we estimated the density of the dusty fluid ($\sim$3.4 kg m^{-3}) and the dynamic viscosity of the dusty gas phase μ_f^{**} (14.5×10^{-5} kg m^{-1} s^{-1}).

Thus, the theoretical hindered settling velocity of the median diameter of particles transported in the middle zone is expected to be as low as 0.35–0.4 m s^{-1} (for the Syamlal–O'Brien and Gidaspow models, respectively). By contrast, direct measurements of the average settling velocity in the middle zone of 1.7 m s^{-1} are four times higher than this theoretical estimate, illustrating the importance of the drag reduction of mesoscale clusters.

Data availability. The data that support the findings of this study are available from the corresponding author upon request.

References

31. Thielicke, W. & Stamhuis, E. J. PIVlab-towards user-friendly, affordable and accurate digital particle image velocimetry in MATLAB. *J. Open Res. Software* **2,** e30 (2014).
32. Wohletz, K. H. Pyroclastic surges and compressible two-phase flow. *Dev. Volcanol.* 247–312 (1998).
33. Marble, F. E. Dynamics of dusty gases. *Annu. Rev. Fluid Mech.* **2,** 397–446 (1970).
34. Pope, S. B. *Turblent Flows* (Cambridge Univ. Press, 2000).